ARTICLE   OPEN

Functional polymeric passivation-led improvement of bias stress with long-term durability of edge-rich nanoporous MoS$_2$ thin-film transistors

Heekyeong Park[1,2,7], Junhwan Choi [3,7], Junoh Shim[2], Seung Min Lee[3], Sungmin On[4], Hyung Joong Yun[5], Sunkook Kim [2✉], Sung Gap Im [3✉] and Hocheon Yoo [6✉]

Nanoporous patterning of two-dimensional materials using block copolymer lithography has drawn much attention. Lateral edge exposures made by the nanoporous patterning provide electrical and optical characteristics that are different from the original materials. However, nanopatterning processes inevitably generate edge exposure and surface defects that may result in poor reliability and reproducibility of the devices. In this study, we propose a reliable method to passivate nanoporous molybdenum disulfide (MoS$_2$) thin-film transistors (TFTs) using polymer thin films, synthesized by initiated chemical vapor deposition (iCVD) to improve the electrical stability of nanoporous MoS$_2$ TFTs. To this end, functional polymer films of electron-donating poly(1-vinylimidzole) (pVI) and inert poly(1H,1H,2H,2H-perfluorodecyl methacrylate) (pPFDMA) were utilized as passivation layers on nanoporous MoS$_2$ TFTs. An n-type doping effect was observed in the pVI-deposited nanoporous MoS$_2$ film due to the electron-donating imidazole ring, whereas the inert pPFDMA efficiently stabilized the electrical characteristics of the nanoporous MoS$_2$ TFTs. Moreover, the hydrophobic fluoroalkyl chain of the pPFDMA film efficiently prevented oxygen and moisture adsorption on the nanoporous MoS$_2$. The superior passivation effect of the pPFDMA layer was confirmed using gate-bias stress tests and long-term storage tests under ambient conditions.

INTRODUCTION

Owing to their high carrier mobility, sharp subthreshold slope, and exceptional endurance to mechanical stress, two-dimensional (2D) materials are considered as potential candidates for applications in functional electronics, such as flexible thin-film transistors (TFTs) for active display matrices and integrated circuits[1–3]. Owing to their large surface-to-volume ratio, various 2D material-based sensing devices have been successfully demonstrated in the past decade, including phototransistors[4–6], gas sensors[7,8], and biosensors[9,10].

The unique electrical and optical properties of 2D materials can be systematically tuned using structural engineering, making 2D materials ideal for electronic devices. Modifying the dimensions or morphology of 2D materials changes their structural properties, which imparts various exotic properties to overcome existing material limitations[11]. As a well-known example, the zero bandgap of pristine 2D graphene does not exhibit good capability for electronic applications. However, it has been modified to form nanodot[12], nanoribbon[13], and nanomesh[14], achieving a finite bandgap. The nanoribbon and nanomesh graphene TFTs also exhibited superior electrical switching properties. Moreover, Kim et al.[15] demonstrated the potential to overcome the low photoluminescence of molybdenum disulfide (MoS$_2$) with an indirect bandgap by patterning the 2D materials to nanopore sheets.

Block copolymer (BCP) lithography is considered a facile but highly effective scheme for constructing nanostructured 2D

materials. The self-assembled nature of BCP can provide large-area uniform patterning with regular nanosized features[16–18]. The simple BCP-based lithography process can obtain high-quality nanopatterns with various shapes without using complex, high-cost processes, such as electron beam (e-beam) irradiation. While the pristine 2D materials are comprised of van der Waals surface without any lateral edge regions, the nanostructured 2D materials made by periodically removing the layer to the size of nanometers provide the lateral edge exposures that the pristine 2D materials fundamentally cannot have. The lateral edge exposures exhibit unique properties; depending on the edge exposure structure (i.e., armchair and zigzag edges), the interaction of electron and phonon can be controlled[19] or oxygen reduction reaction catalysts can be obtained[20]. The mentioned lateral edge exposures have been expanding the development of various applications such as optoelectronics, chemical and biomedical sensing, and catalytic activity[14,15,21,22]. Admittedly, nanopatterning can improve device performance. However, there is a severe disadvantage related to the lack of electrical stability, which results from the edge exposure and structural defects caused by the nanopatterning process. It is well known that the surface edges and defects on 2D materials are highly sensitive to oxygen and moisture in ambient environment[23]. Consequently, the adsorption of oxygen and moisture on the nanopatterned surface acts as charge trap sites, limiting electron transport, which changes the electrical characteristics of the devices[24] and causes hysteresis due to charge trapping or release[25]. Therefore, it is essential to passivate the

[1]Harvard Institute of Medicine, Harvard Medical School, Harvard University, Brigham and Women's Hospital, Boston, MA 02115, USA. [2]Department of Advanced Materials Science and Engineering, Sungkyunkwan University (SKKU), Suwon 16419, Republic of Korea. [3]Department of Chemical and Biomolecular Engineering, Korea Advanced Institute of Science and Technology (KAIST), Daejeon 34141, Republic of Korea. [4]Pohang Accelerator Laboratory, Pohang 37673, Republic of Korea. [5]Research Center for Materials Analysis, Korea Basic Science Institute (KBSI), Daejeon 34133, Republic of Korea. [6]Department of Electronic Engineering, Gachon University, Seongnam 13120, Republic of Korea. [7]These authors contributed equally: Heekyeong Park, Junhwan Choi. ✉email: seonkuk@skku.edu; sgim@kaist.ac.kr; hyoo@gachon.ac.kr

nanopatterned surface efficiently from external contaminants using an appropriate passivation layer without damaging the 2D semiconductor.

Various inorganic and organic layers have been employed for the passivation of 2D materials using several deposition methods, including atomic layer deposition (ALD)[26,27], pulsed laser deposition[28], and solution-based deposition[29,30]. However, these methods can induce damage and degradation on the channel surface and affect the electrical performance of nanopatterned TFTs. The deterioration in performance is caused by the susceptibility of the unstable edges and defects of the nanopatterned surface to high temperatures and solvent environments.

In this study, we propose polymeric passivation of a nanopatterned MoS$_2$ TFT via initiated chemical vapor deposition (iCVD). The vapor-phase process enables solvent-free, near-room-temperature deposition of polymer thin films without damaging or changing the electrical characteristics of the underlying 2D materials[31]. In contrast, conformal coverage of 2D material surfaces without perturbation is challenging in conventional ALD and solution-based deposition, primarily because such deposition processes are highly dependent on the surface chemical properties or prone to damage from solvent[32,33]. Moreover, ultrathin polymer films can be deposited conformally on any arbitrary 2D material surface because, during the iCVD process, the polymer film grows on the substrate surface from the input monomers adsorbed thereon[34,35]. We employed two different polymer films of poly(1-vinylimidzole) (pVI) and poly(1H,1H,2H,2H-perfluorodecyl methacrylate) (pPFDMA) to passivate nanoporous MoS$_2$ TFTs. We confirmed conformally deposited polymer layers on the nanoporous MoS$_2$ and the corresponding electrical and chemical changes in the MoS$_2$ using Raman spectroscopy, ultraviolet photoelectron spectroscopy (UPS), scanning transmission electron microscopy (STEM), X-ray photoelectron spectroscopy (XPS), atomic force microscopy (AFM), and current measurements. Remarkably, the deposition of the inert pPFDMA layer on the nanoporous MoS$_2$ exhibited exceptional passivation performance under repeated gate-bias stress and long-term air exposure, which enabled the long-term stable operation of the nanoporous MoS$_2$ TFT.

RESULTS AND DISCUSSION

Chemical and morphological properties of nanoporous MoS$_2$

Figure 1a shows a schematic illustration of a fabrication process of nanoporous MoS$_2$. The multilayer MoS$_2$ films were transferred onto a Si/SiO$_2$ substrate by a mechanical exfoliation from bulk. A 10 nm-thick SiO$_2$ was deposited onto the MoS$_2$ surface to prevent surface damage of the MoS$_2$ during the patterning process. Random copolymer (RCP) was spin-coated onto the SiO$_2$ surface before the BCP coating to improve wetting interactions between the solid substrate and the BCP layer. The BCP layer was self-assembled under annealing at 230 °C and a periodic nanohole pattern was obtained by selective decomposition of polymer block located in the inner holes. A hexagonally packed cylindrical BCP film (Supplementary Fig. 1) was utilized as a lithographic mask to fabricate the periodic nanoholes on the multilayer MoS$_2$. The underlying RCP, SiO$_2$, and MoS$_2$ were sequentially perforated by O$_2$, SF$_6$, and BCl$_3$ plasma reactive ion etching (RIE), respectively. Finally, remained RCP and SiO$_2$ layers were removed by immersing the substrate in buffered oxide etchant (BOE).

The morphological and chemical properties of nanoporous MoS$_2$ were explored using STEM, Raman spectroscopy, and XPS analyses. Figure 1b illustrates a STEM image of the perforated multilayer MoS$_2$ with periodic nanohole arrays on its surface. The average hole diameter of the MoS$_2$ nanoholes was 24.29 ± 1.99 nm. A cross-sectional STEM image showed vertically organized nanoholes across nine MoS$_2$ layers (Fig. 1c). Figure 1d illustrates a STEM image of the hexagonally packed nanoholes on

the MoS$_2$. The atomic configurations in the exposed edge area consist of both arm-chair and zigzag arrangements of Mo and S atoms (Fig. 1e), which may be formed by anisotropic etching under the BCl$_3$ plasma RIE.

Raman spectroscopy and XPS analyses were conducted to investigate the electronic and chemical structure of the nanoporous MoS$_2$. In the Raman spectra (Fig. 1f), two Raman peaks of in-plane (E^1_{2g}) and out-of-plane (A_{1g}) vibration modes were observed at 382 and 407 cm^{-1}, respectively. The measured Raman peak intensity of A_{1g} was 2.04 times higher than that of E^1_{2g} because the vibration of A_{1g} is preferentially promoted to the E^1_{2g} vibration for the edge-exposed MoS$_2$[15,21,36]. Furthermore, a small peak was also observed at 226 cm^{-1}, corresponding to a defect-induced longitudinal acoustic vibration at the M point of the Brillouin zone (LA(M))[37,38]. The Raman scattering mentioned above was rarely observed in the pristine MoS$_2$, whereas it was activated considerably on the perforated MoS$_2$ films owing to the abundant edge defects.

The XPS spectra of the nanoporous MoS$_2$ are shown in Fig. 1g, h with respect to the core atoms of Mo and S. The spectrum of Mo 3d was deconvoluted into three components. The peaks located at 232.4 and 235.53 eV can be assigned to Mo^{6+} 3$d_{5/2}$ and Mo^{6+} 3$d_{3/2}$, respectively, indicating the existence of MoO$_3$[39]. The atomic fraction of Mo^{6+} 3d among the total Mo ligands was approximately 10.4%. The strong doublet at 229.19 and 232.32 eV corresponding to Mo^{4+} 3$d_{5/2}$ and Mo^{4+} 3$d_{3/2}$ of intrinsic MoS$_2$ (i-MoS$_2$) represented a stoichiometric Mo-S bonding (ratio of S/Mo = 2)[40]. However, nanoporous MoS$_2$ involves many broken bonds at edge sites. The nonstoichiometric Mo-S bonding (ratio of S/Mo <2) was referred to the defective MoS$_2$ (d-MoS$_2$) peaks located at 228.59 eV (Mo^{4+} 3$d_{5/2}$) and 231.72 eV (Mo^{4+} 3$d_{3/2}$)[40]. The atomic fraction of d-MoS$_2$ (16%) was higher than that of MoO$_3$. The result indicates that many edge atoms were present with dangling bonds rather than in the oxidized form. For the S 2p spectra, two peaks were observed at 162 and 163.18 eV, corresponding to S^{2-} 2$p_{3/2}$ and S^{2-} 2$p_{1/2}$, respectively, which is attributable to Mo-S bonding[39]. No defective peak was observed in the S 2p spectra owing to the low energy resolution at low binding energy levels.

Polymeric passivation of nanoporous MoS$_2$

Figure 2a shows a schematic of the polymer deposition process on the nanoporous MoS$_2$ surface. In the iCVD process, the injected monomers are adsorbed to the cooled substrate, and initiators are decomposed to form radicals by the heated filament at a temperature of less than 200 °C. It triggers the growth of the polymeric film on the nanoporous surface[41].

Since the substrate temperature was <40 °C, the solvent-free vapor-phase deposition method can minimize damage to the substrate surface, which is a distinct advantage of the iCVD process, thus rendering the deposition method suitable for damage-free passivation of the nanoporous MoS$_2$. Accordingly, pVI and pPFDMA were selected as candidate layers for the passivation layer of the nanoporous MoS$_2$ TFTs (Fig. 2b). The pVI polymer includes an electron-donating (or electropositive) imidazole ring, which can affect the charge distribution of nanoporous MoS$_2$. Indeed, in our previous study, threshold voltage (V_{TH}) and Dirac voltage (V_{Dirac}) in organic and graphene field-effect transistors could be controlled systematically by exploiting the electron-donating imidazole moiety in the pVI-containing layer[42,43]. Meanwhile, pPFDMA contains an inert, long perfluoroalkyl chain. Ultrathin (~70 nm) pVI and pPFDMA layers were deposited directly on the nanoporous MoS$_2$ TFT device, as shown in the high-resolution transmission electron microscopy (HRTEM) images and electrical characteristics of the polymer films (Supplementary Figs. 2 and 3 and Supplementary Table 1). Owing to the mild deposition conditions, the chemical functionalities including imidazole and fluoroalkyl moieties in each monomer
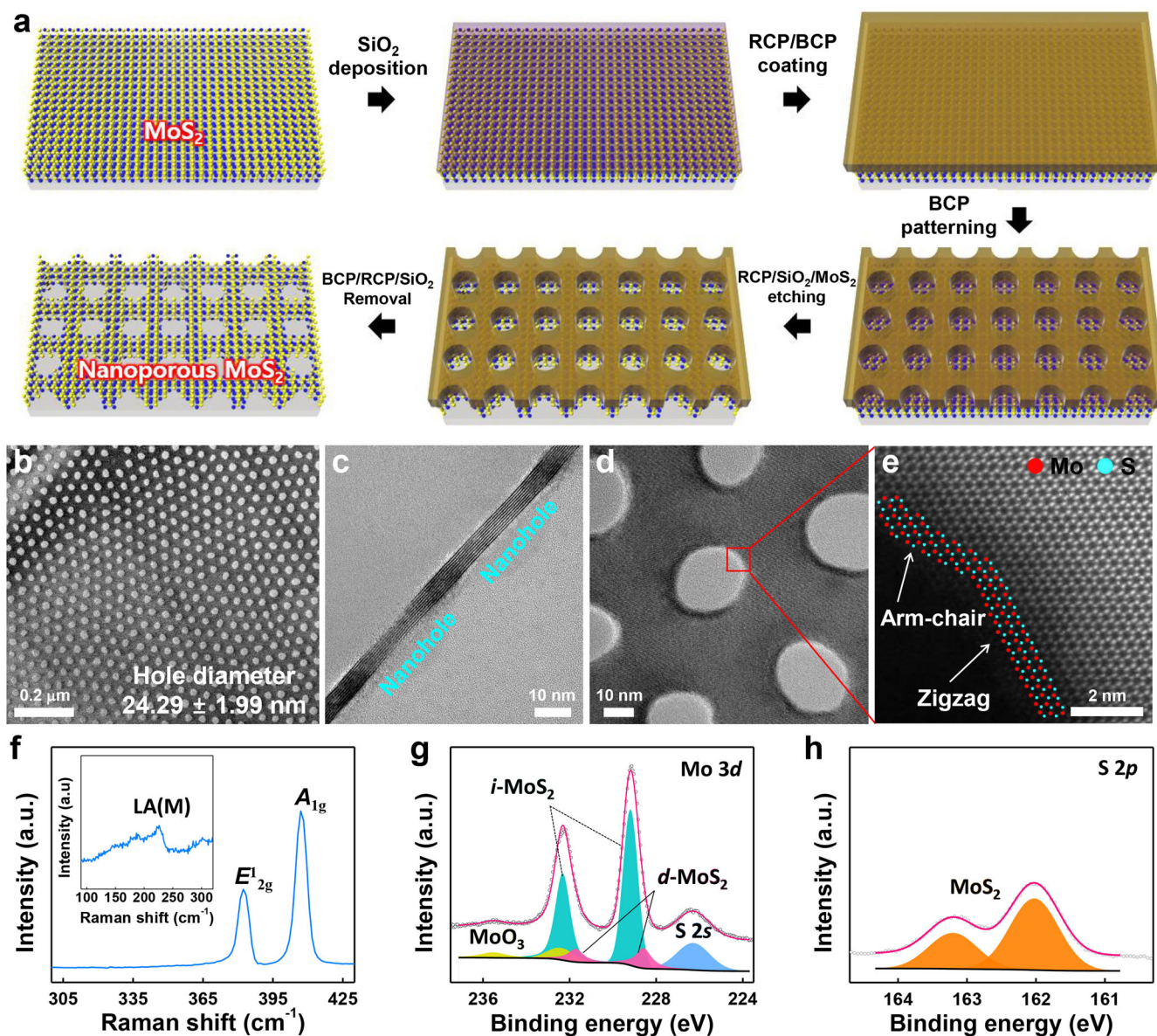
Fig. 1 **Fabrication and observation of nanoporous MoS2 film. a** Schematic illustration of the fabrication process of nanoporous MoS2. **b** Low-magnification STEM image and **c** cross-sectional view of nanoporous MoS2. **d** STEM image representing the hexagonally packed nanohole array. **e** Atomic configuration of the exposed edge in nanoporous MoS2. **f** Raman and **g, h** XPS spectra of nanoporous MoS2.

were fully preserved in the resulting polymer film on the MoS2 surface, which was confirmed by Fourier transform infrared (FTIR) spectroscopy (Supplementary Fig. 4).

Raman spectroscopy and UPS analyses were performed to investigate the variation in the electrical characteristics of the nanoporous MoS2 films with each polymer passivation layer (Fig. 2c–e). The pristine nanoporous MoS2 films exhibited E^1_{2g} and A_{1g} peaks at 382 and 407 cm^{-1} [44], respectively. The pVI-passivated nanoporous MoS2 showed a remarkable bathochromic shift in both vibration modes (Fig. 2c), whereas no apparent peak shift was observed from the pPFDMA-deposited nanoporous MoS2 film (Fig. 2d). We also performed the Raman analysis on the non-patterned MoS2 with the polymer passivation layers (Supplementary Fig. S5). The pVI layer induced a negative shift of A_{1g} peak of the non-patterned MoS2. Since the Raman peaks of non-passivated MoS2 have a much higher intensity than the nanoporous MoS2, the shift seems to be relatively small. In

addition, the shift of E^1_{2g} was not observed because it is less sensitive to electron doping than the A_{1g} vibration mode[45]. On the other hand, no apparent peak shift was observed in the inert pPFDMA passivation on the MoS2 regardless of the surface structures. The UPS spectra of pristine and polymer-passivated nanoporous MoS2 are shown in Fig. 2e. The work function (ϕ) can be calculated using $\phi = h\nu - W$, where $h\nu = 21.2$ eV and W denotes the secondary electron cut-off ($E_{cut-off}$)[46]. The $E_{cut-off}$ of the nanoporous MoS2 was shifted toward higher binding energy with the pVI passivation layer, resulting in a lower ϕ value of the pVI-passivated nanoporous MoS2 (3.24 eV) than that of the pristine nanoporous MoS2 (4.03 eV) (Fig. 2f). Meanwhile, the pPFDMA-passivated nanoporous MoS2 only exhibited a marginal increase in ϕ toward 4.10 eV, resulting from electronegative fluoroalkyl side chain[47,48]. These results were derived from the distinct electrical properties of the two polymers. The electron-donating group in the pVI polymer induced an n-doping effect[42], while the inert
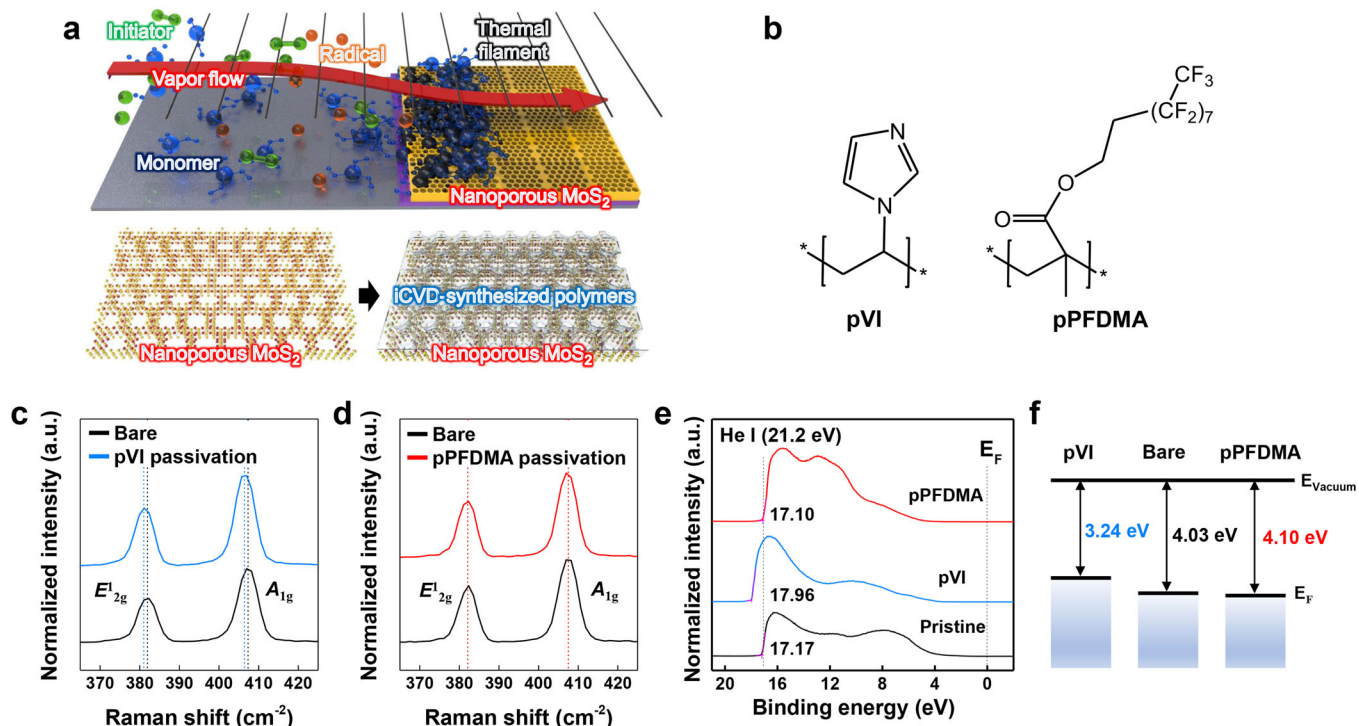
Fig. 2 Polymeric passivation of nanoporous MoS₂ films using pVI and pPFDMA, respectively. a Schematic illustration of the passivation of nanoporous MoS₂ by iCVD process and **b** chemical structures of passivation layers. **c, d** Raman spectra and **e** UPS spectra of the pVI- and pPFDMA-passivated nanoporous MoS₂ compared to the pristine one. **f** Energy band structures of the polymer-passivated nanoporous MoS₂ compared to the pristine one calculated from the UPS analysis.

fluoroalkyl chain in pPFDMA induced an insignificant p-doping effect. The similar electrical effects of two polymer layers were observed in the UPS analysis on the non-patterned MoS₂ without nanoporous structure (Supplementary Fig. 6a, b), which represents highly coherent electrical properties of the polymers on the MoS₂ films regardless of the surface structures.

Characterization of polymer-passivated nanoporous MoS₂ film

In this study, we conducted high-angle annular dark-field (HAADF)-STEM analysis on the polymer-deposited MoS₂ film to confirm the effective passivation of two different polymer layers on the nanoporous MoS₂. Cross-sectional HAADF-STEM images with energy dispersive spectroscopy (EDS) mapping are shown in Fig. 3a–j. Both pVI and pPFDMA passivation layers were deposited conformally on the nanoporous MoS₂ surface without any notable defects (Fig. 3a, f). The EDS mapping illustrates a uniform distribution of C and N (pVI) or C and F (pPFDMA), which are clearly distinguishable from underlying Mo and S. The surface chemical composition of the pVI- and pPFDMA-passivated nanoporous MoS₂ was investigated by XPS and compared with that of pristine nanoporous MoS₂ (Fig. 3k).

Accordingly, Mo $3d$ and S $2p$ peaks were detected in the XPS survey spectrum of pristine nanoporous MoS₂. Moreover, Si- and O-related peaks were also detected, which resulted from the Si/SiO₂ substrate. In the polymer-passivated nanoporous MoS₂, the intensities of the Mo $3d$ and S $2p$ peaks were smaller than those of pristine MoS₂. Evidently, the C $1s$ and N $1s$ peak intensities increased in the pVI-passivated nanoporous MoS₂, and the increased intensities of C $1s$ and F $1s$ peaks were obtained in the pPFDMA-passivated nanoporous MoS₂. In fact, the XPS analysis clearly revealed that the polymer passivation layer conformally covered the nanoporous MoS₂ surface, which is completely consistent with the cross-sectional HAADF-STEM images.

To further investigate the surface properties of the polymer-passivated nanoporous MoS₂, AFM analysis was performed (Fig. 3l). The AFM image of the pristine nanoporous MoS₂ clearly exhibited porous structure and the smooth, amorphous surface morphology was confirmed with the root-mean-square roughness (R_q) <0.5 nm, which also indicates that the pVI layer conformally covered the nanoporous MoS₂. On the other hand, the AFM image of the pPFDMA-passivated nanoporous MoS₂ exhibited the roughened surface with the R_q value >15 nm. This rough surface morphology was originated from the highly crystalline nature of pPFDMA due to the fluoroalkyl chain[49], which can also improve the hydrophobicity of the surface[50,51]. The water contact angle (WCA) analysis also verified that the surface property of the nanoporous MoS₂ was controlled according to the deposition of the polymer films (Supplementary Fig. 7). Therefore, it follows from the comprehensive analyses that the vapor-phase-deposited polymer passivation layers conformally covered the nanoporous MoS₂ surface without incurring defect or damage to the underlying MoS₂, while fully retaining the chemical functionalities of each polymer film.

**Electrical characteristics of nanoporous MoS₂ TFTs passivated by pVI and pPFDMA polymers**

To investigate the passivation effect of the pVI and pPFDMA layers on the nanoporous MoS₂ TFTs, we measured the electrical characteristics of the devices before and after the passivation with each polymer layer. Figure 4a, b show a schematic illustration and an optical image of the polymer-passivated nanoporous MoS₂ TFT, respectively. Figure 4c, d show the transfer curves of the pVI- and pPFDMA-passivated nanoporous MoS₂ TFTs, respectively. The transfer curves are compared with those of the bare MoS₂ TFT. Optical images of the MoS₂ devices after the deposition of each polymer are depicted in Supplementary Fig. 8. The curves are plotted in both logarithmic and linear scales under a gate voltage

(V_{GS}) window ranging from −40 to 40 V and drain voltage (V_{DS}) of 1 V. A hysteresis between forward and reverse V_{GS} sweeps was suppressed when the MoS_2 surfaces were passivated using both polymer layers, indicating that charge trapping on the MoS_2 edge–air interface was efficiently prevented by the polymer passivation. Following the deposition of the pVI polymer on the nanoporous MoS_2 TFT, a significant increase was observed in the drain current (I_{DS}) in depletion regions and a slight increase in the accumulation region (Fig. 4c). In addition, a negative V_{TH} shift of −8.4 V was detected. Meanwhile, the deposition of pPFDMA only exhibited a marginal shift in the transfer curve, except for a small decrease in the on-current (Fig. 4d). The variations in V_{TH} and on–off ratio ($I_{on/off}$) were monitored for 12 and 15 MoS_2 TFTs passivated with each pVI and pPFDMA layer, respectively (Supplementary Fig. 9a–d and Fig. 4e). For comparison, we defined that the current level at V_{GS} of −40 V is off-current, even if the pVI-deposited MoS_2 TFT showed metallic behavior. Generally, a strong difference was observed in V_{TH} and $I_{on/off}$ before and after the deposition of pVI; in contrast, the variation was insignificant in the case of the pPFDMA-passivated device. The n-doping behavior of the pVI-deposited nanoporous MoS_2 TFT can be attributed to the electron-donating effect of the imidazole ring in pVI (Fig. 4f). On the other hand, the long fluoroalkyl chain provided a strong hydrophobicity on the polymer passivation layer[51], which effectively prevented oxygen and water adsorption, which, in turn, minimized the perturbation of the electrical characteristics of the nanoporous MoS_2 TFTs (Fig. 4g). In other words, the pPFDMA layer can effectively passivate the nanoporous MoS_2 surface with little change in the electrical characteristics of the TFT devices. Additionally, we extracted field-effect mobilities of 12 and 15
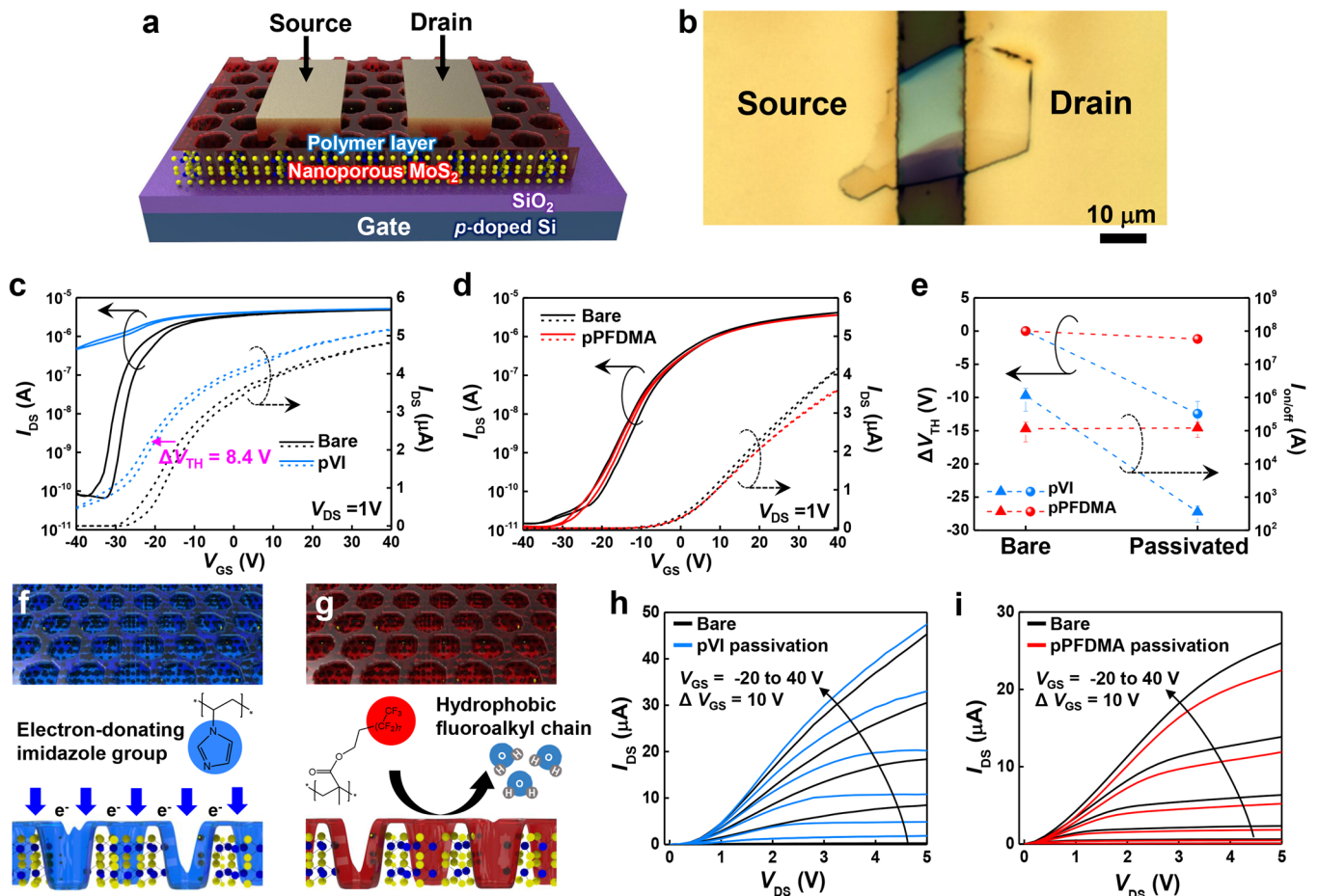
nanoporous MoS_2 TFTs before and after pVI and pPFDMA polymer passivation (Supplementary Fig. 9e, f), respectively. We calculated the mobility variation using an equation of ($\mu_{after} - \mu_{before}$)/$\mu_{before} \times 100$ (%), where μ_{before} and μ_{after} are the field-effect mobility values measured before and after the passivation, respectively. The average variations for pVI and pPFDMA are calculated as −2.1 and −1.4%, respectively. Such small variations indicate that the polymer layers rarely induce the carrier scattering at the interface between the nanoporous MoS_2 and the polymer. In the output curves measured under V_{GS} range from −20 to 40 V with an interval of 10 V, the increase in I_{DS} was more prominent in the lower range of V_{GS} than the higher range for pVI-deposited nanoporous MoS_2 TFT, which conforms with the observation in the corresponding transfer curve. However, a practically identical shape of the output curve was observed for the pPFDMA-deposited device, except for a slight decrease in I_{DS} in positive V_{GS} ranges.

Stability tests of pPFDMA-passivated nanoporous MoS_2 TFTs

The pPFDMA layer grown by iCVD provided an outstanding passivation effect on the nanoporous MoS_2 by benefitting from its non-electrostatic properties and its ability to prevent the adsorption of water molecules from the air. We conducted gate-bias stress tests and long-term storage tests under ambient air conditions to examine the passivation performance of the pPFDMA layer on the nanoporous MoS_2 TFTs. Positive bias stress (PBS), negative bias stress (NBS), positive bias illumination stress (PBIS), and negative bias illumination stress (NBIS) under a white light source of 1500 lux were conducted (Fig. 5a–d). V_{GS} of 30 and
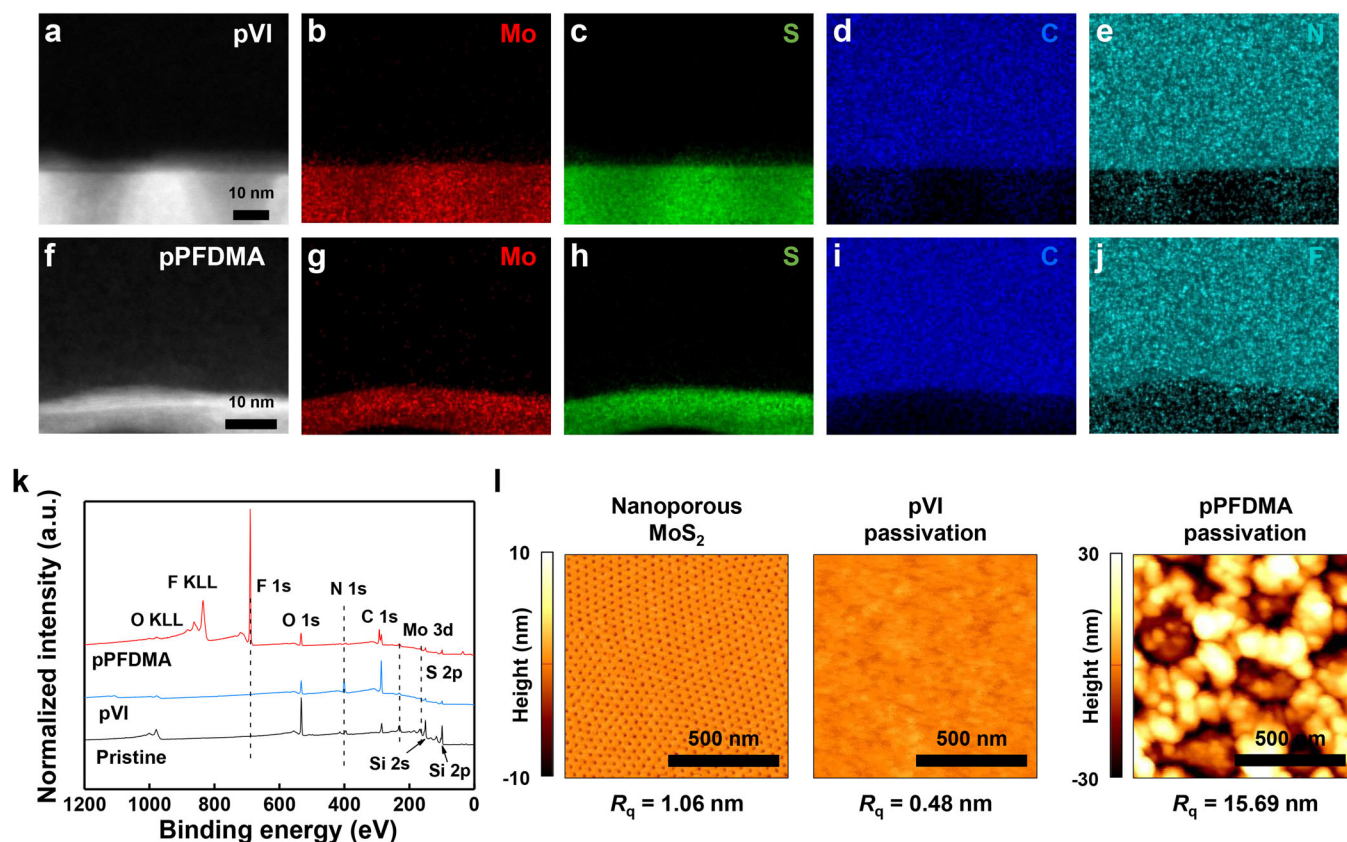
Fig. 3 Chemical and morphological properties of polymer-passivated nanoporous MoS_2 films. HAADF-STEM images and EDS elemental mapping of the **a-e** pVI- and **f-j** pPFDMA-passivated nanoporous MoS_2. False color modification was attempted in EDS elemental mapping images to clearly reveal the polymeric passivation layers and nanoporous MoS_2. **k** XPS survey scan spectra of the pristine and polymer-passivated nanoporous MoS_2. The N1s and F1s peaks were detected only in the pVI- and pPFDMA-passivated nanoporous MoS_2. **l** AFM images of the polymer-passivated nanoporous MoS_2 as well as the pristine one.

Fig. 4 Electrical properties of polymer-passivated nanoporous MoS₂ TFTs. a Schematic and **b** optical images of polymer-passivated nanoporous MoS₂ TFT. Transfer characteristics of the nanoporous MoS₂ TFT before and after deposition of **c** pVI and **d** pPFDMA films. **e** Variation in V_{TH} and $I_{on/off}$ of the nanoporous MoS₂ TFTs after passivation with pVI and pPFDMA layers, respectively. Schematic of electrical behavior at polymer/MoS₂ interface when passivated with **f** pVI and **g** pPFDMA layers, respectively. Output curves of **h** pVI- and **i** pPFDMA-deposited nanoporous MoS₂ TFTs together with the corresponding non-passivated TFTs.

−22 V were applied as positive and negative gate stress voltages (V_{Stress}), respectively. We measured the transfer curves every 10 min while giving bias stress for a total stress time of 120 min as shown in Supplementary Fig. 10. These bias stress tests were also conducted on the non-passivated nanoporous MoS₂ control TFT to facilitate comparison, as shown in Supplementary Fig. 11a–d. Compared to the positive V_{TH} shift of the non-passivated MoS₂ TFT under the PBS test, no appreciable V_{TH} change was observed in the passivated TFT (Fig. 5a), suggesting that the pPFDMA passivation layer can effectively prevent the charge trapping induced by the adsorption of oxygen or water in an ambient environment at the edge defect sites. In the case of NBS, a slight shift in V_{TH} was observed in the passivated MoS₂ TFT because the electrons pre-trapped at the edge sites in the nanoporous MoS₂ were released under the negative bias stress (Fig. 5b). However, it is worth noting that the variation was considerably smaller than that of the one occurring in the non-passivated device. For the PBIS test, the V_{TH} was positively shifted in the non-passivated nanoporous MoS₂ TFT, while the passivated TFT showed a shift of V_{TH} toward the negative direction, albeit to a minor degree (Supplementary Figs. 11c and 5c). The PBS test indicated that edge sites were efficiently stabilized and the adsorption of oxygen or water molecules can be prevented by pPFDMA passivation. However, the inherent trap states in the nanoporous MoS₂ induced by the edge defects captured the photoexcited hole carriers under illumination, resulting in a positive gating effect

thereby resulting in a small V_{TH} shift toward the negative direction[5,6]. The negative shift was significantly activated under the NBIS test, in which the electron release and hole trapping in the trap states of the nanoporous MoS₂ occur simultaneously. Figure 5e shows the shift in V_{TH} of the nanoporous MoS₂ TFT passivated and non-passivated by the pPFDMA layer at each measurement, where the variation of the passivated devices is quite small compared to that for the non-passivated TFT.

Furthermore, a long-term storage test was conducted to validate the robustness of the pPFDMA-passivated nanoporous MoS₂ TFT under exposure to an ambient environment. The average V_{TH} shift of the pPFDMA-passivated nanoporous MoS₂ TFTs was monitored over 40 days with 5-day interval, compared to the non-passivated one (Fig. 5f). The raw transfer curves of each representative device are shown in Supplementary Fig. 12. The V_{TH} of the non-passivated devices was positively shifted with time owing to the electron trapping induced by the adsorption of oxygen and water molecules on the nanoporous MoS₂ surface. It is well known that the energetically unstable broken bonds located at the edges of the nanoporous MoS₂ channel surface prompt the adsorption of oxygen and moisture far more than normal MoS₂, which inevitably deteriorates the device performance[52,53]. In contrast, the nanoporous MoS₂ passivated by pPFDMA does not show appreciable device degradation and has a negligible V_{TH} shift, which verifies the excellent passivation performance of the
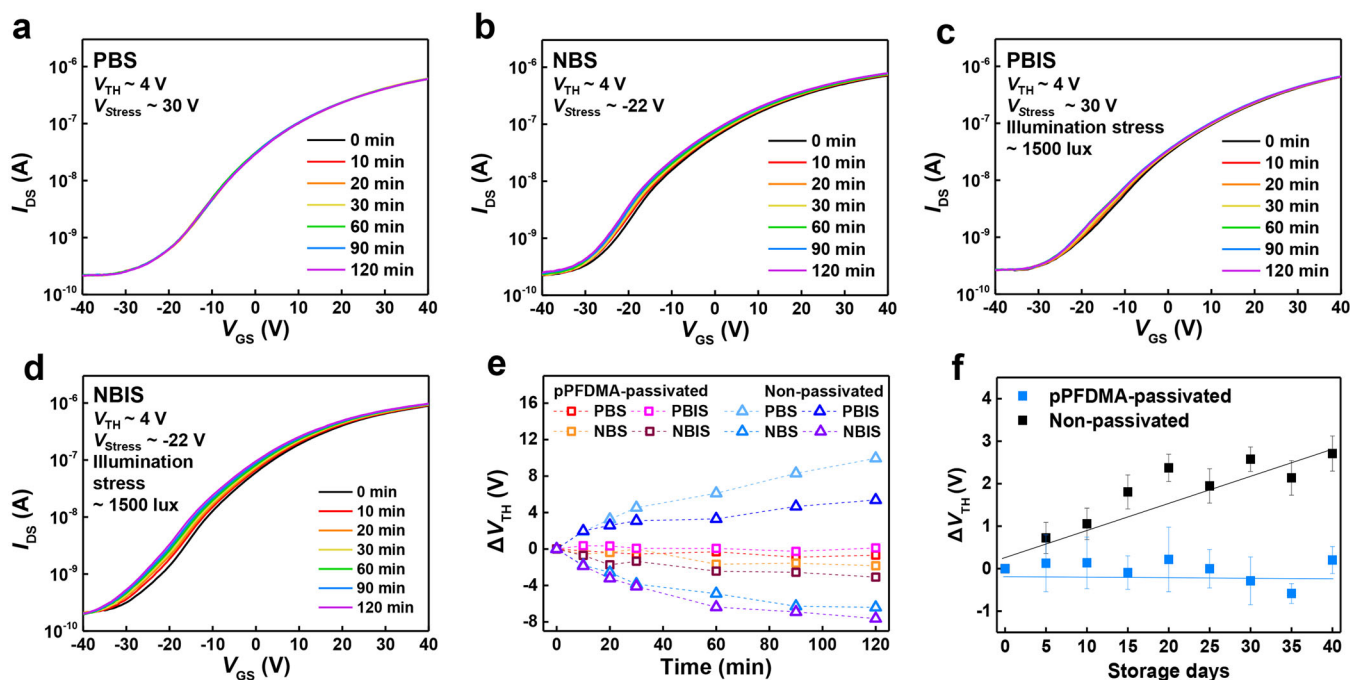
Fig. 5 Gate bias and illumination stress tests and long-term storage test of pPFDMA-passivated nanoporous MoS$_2$ TFTs. Transfer characteristics of the pPFDMA-passivated nanoporous MoS$_2$ TFT under **a** PBS, **b** NBS, **c** PBIS, and **d** NBIS conditions with positive bias stress of 30 V and negative bias stress of −22 V. A light source of 1500 lux was used for the illumination stress. **e** Variation of V_{TH} of nanoporous MoS$_2$ TFT passivated with pPFDMA layer and non-passivated one according to the stress time. **f** Long-term storage test of pPFDMA-passivated and non-passivated nanoporous MoS$_2$ TFTs under exposure in the ambient environment.

pPFDMA polymer synthesized by the iCVD process for robust nanoporous MoS$_2$ devices.

In summary, we demonstrated an efficient passivation method for nanoporous MoS$_2$ using polymeric passivation layers via iCVD process. The proposed solvent-free method effectively passivated the surface edges and defects in nanoporous MoS$_2$, without damaging or degrading its structure and electrical integrity. The pVI with an electron-donating imidazole ring and pPFDMA containing a fluoroalkyl chain were utilized as n-doping and inert polymer passivation layers, respectively. Both polymer passivation layers conformally covered the underlying nanostructured MoS$_2$. The nanoporous MoS$_2$-based TFT with the polymer passivation layers showed a significant negative V_{TH} shift in the pVI-deposited nanoporous MoS$_2$ TFT, whereas the pPFDMA-deposited nanoporous MoS$_2$ TFT only exhibited a small reduction in the on-current. On the other hand, the long fluoroalkyl chain in the pPFDMA provided strong hydrophobicity, thus remarkably enhancing the stability of the nanoporous MoS$_2$ TFT in ambient air. The pPFDMA-deposited nanoporous MoS$_2$ TFT demonstrated outstanding stability in the PBS, NBS, PBIS, and NBIS tests compared to the non-passivated device, primarily because the pPFDMA can efficiently abate the water and oxygen adsorption on the nanoporous MoS$_2$ surface. In addition, only a negligible change was observed in the long-term storage test, which confirms the robustness of the pPFDMA-deposited nanoporous MoS$_2$ TFT. We believe that this study can provide an effective strategy for the passivation of nanostructured 2D materials. In particular, a vapor-phase deposited fluoropolymer can enhance the ambient stability of nanostructured 2D materials-based TFTs, without damaging their electrical characteristics.

METHODS

Fabrication of nanoporous MoS$_2$ TFTs
Multilayer MoS$_2$ nanosheets were mechanically exfoliated from bulk MoS$_2$ and transferred onto Si/SiO$_2$ substrates. The substrate was then placed in acetone overnight and washed with isopropyl alcohol for surface cleaning. A 10 nm-thick SiO$_2$ layer was deposited onto the surface of MoS$_2$ using the e-beam evaporator. Subsequently, the substrate was spin-coated with a 1 wt% toluene solution of poly (styrene-r-methyl methacrylate) (PS-r-PMMA) ($M_n = 8500$ $M_w/M_n = 1.45$, styrene content 66%, α-hydroxy-ω-TEMPO moiety terminated) RCP, at a speed of 3000 rpm. The substrate was annealed at 250 °C for 2 hours under vacuum and washed with toluene. Next, the substrate was spin-coated with a 1 wt% toluene solution of poly (styrene-b-methyl methacrylate) (PS-b-PMMA) (PS:PMMA = 55,000:22,000, $M_w/M_n = 1.09$) BCP at a speed of 3000 r.p.m. and annealed at 230 °C for 2 h under vacuum conditions. The substrate was exposed to 254 nm ultraviolet irradiation for 30 min and placed in acetic acid for 15 min to decompose the PMMA section in the BCP thin film. O$_2$ plasma RIE (10 sccm, 50 W, 4 s) was used to etch the RCP layer and control the nanohole size. Next, SF$_6$ plasma RIE (10 sccm, 200 W, 20 s) was performed to create nanoholes on the SiO$_2$ layer. BCl$_3$ plasma RIE (15 sccm, 100 W) was utilized to fabricate nanoporous MoS$_2$ by controlling the treatment time, depending on the thickness of MoS$_2$. The final process of making nanoporous MoS$_2$ involved immersing the substrate in BOE for 3 s to remove the SiO$_2$ layer. The source and drain were prepatterned using photolithography to fabricate the nanoporous MoS$_2$ TFT, and Ti and Au (20 nm/100 nm) were deposited on the nanoporous MoS$_2$.

Synthesis of polymer films
1-Vinylimidzole (VI) (≥99%), 1H,1H,2H,2H-perfluorodecyl methacrylate (PFDMA) (97%) monomers and $tert$-butyl peroxide (TBPO) (98%) initiator were purchased from Sigma-Aldrich. The polymer passivation layers were deposited using a custom-built iCVD system. For the deposition of pVI, VI monomer and TBPO initiator were injected into the chamber at flow rates of 4.4 and 1.5 sccm, respectively. The chamber pressure was maintained at 450 mTorr. For the deposition of pPFDMA, PFDMA monomer and TBPO initiator were injected into the chamber at flow rates of 0.2 sccm, and the chamber pressure was maintained at 40 mTorr. For both polymer film depositions, the substrate temperature was maintained at 40 °C, and the filament was heated to 130 °C to decompose the initiator into radicals.

Characterization

Raman measurements were carried out using a micro-Raman spectrometer system (ALPHA300, WITec) with a green excitation laser. Energy band structure analysis was performed using UPS (AXIS SUPRA, Kratos. Inc.) from the Korean Basic Science Institute (KBSI). UPS was performed using a He I ($hv = 21.2$ eV) source from a gas discharge lamp. Plan-view and cross-sectional STEM images of the nanoporous MoS_2 were obtained using a STEM measurement system (HD-2300A, Hitachi) with an accelerating voltage of 200 kV. Ion milling for the cross-sectional image was conducted using a single-beam focused ion-beam (FB-2100, Hitachi). For electrical characterization of the polymer films, 50 nm-thick Al electrode was thermally deposited under high vacuum $<2 \times 10^{-6}$ torr and the polymer films were deposited between top and bottom Al electrode to fabricate the metal–insulator–metal structure. The XPS spectra of the nanoporous MoS_2 were obtained using K-Alpha (Thermo Fisher Scientific) with monochromated Al Ka radiation. FTIR spectra were obtained by an ALPHA FTIR (Bruker Optics) in the absorbance mode to analyze the chemical composition. The AFM images were obtained using a scanning probe microscope (XE-100, Park Systems) to analyze the surface morphology of the nanoporous MoS_2 and polymer films. The WCA analysis was performed using a contact angle measurement system (Phoenix Series, S.E.O.). The device was sliced by a focused ion beam (Helios Nanolab 450, FEI) and the cross-sectional HRTEM images were obtained and analyzed by field emission TEM (Talos F200X, FEI) and EDS mapping to visualize the polymer passivation layers on top of the nanoporous MoS_2. The electrical measurements of the TFTs were performed using a semiconductor characterization analyzer (4200-SCS, Keithley) equipped with a probe station for sample loading and electrode contact. We measured the same devices before and after the polymer passivation. After the measurement of the bare MoS_2 devices, we deposited a polymer layer on the devices and opened the source and drain contacts by etching the local polymer layer using the BOE solution.

DATA AVAILABILITY

The data presented in this study are available from the corresponding author upon reasonable request.

REFERENCES

1. Li, N. et al. Large-scale flexible and transparent electronics based on monolayer molybdenum disulfide field-effect transistors. *Nat. Electron.* **3**, 711–717 (2020).
2. Yu, S. et al. Transition metal dichalcogenide-based transistor circuits for gray scale organic light-emitting displays. *Adv. Funct. Mater.* **27**, 1603682 (2017).
3. Lin, Y. M. et al. Wafer-scale graphene integrated circuit. *Science* **332**, 1294–1297 (2011).
4. Kim, S. G. et al. Infrared detectable MoS_2 phototransistor and its application to artificial multilevel optic-neural synapse. *ACS Nano* **13**, 10294–10300 (2019).
5. Park, H. et al. Exceptionally uniform and scalable multilayer MoS_2 photo-transistor array based on large-scale MoS_2 grown by RF sputtering, electron beam irradiation, and sulfurization. *ACS Appl. Mater. Interfaces* **12**, 20645–20652 (2020).
6. Kim, S. et al. Interstitial Mo-assisted photovoltaic effect in multilayer $MoSe_2$ phototransistors. *Adv. Mater.* **30**, 1705542 (2018).
7. Kim, S. et al. Active-matrix monolithic gas sensor array based on MoS2 thin-film transistors. *Commun. Mater.* **1**, 86 (2020).
8. Schedin, F. et al. Detection of individual gas molecules adsorbed on graphene. *Nat. Mater.* **6**, 652–655 (2007).
9. Park, H. et al. MoS_2 field-effect transistor-amyloid-beta$_{(1-42)}$ hybrid device for signal amplified detection of MMP-9. *Anal. Chem.* **91**, 8252–8258 (2019).
10. Kwong Hong Tsang, D. et al. Chemically functionalised graphene FET biosensor for the label-free sensing of exosomes. *Sci. Rep.* **9**, 13946 (2019).
11. Wang, B. L. et al. Bioelectronics-related 2D materials beyond graphene: fundamentals, properties, and applications. *Adv. Funct. Mater.* **30**, 2003732 (2020).
12. Camilli, L. et al. Self-assembly of ordered graphene nanodot arrays. *Nat. Commun.* **8**, 47 (2017).
13. Chen, Y. C. et al. Tuning the band gap of graphene nanoribbons synthesized from molecular precursors. *ACS Nano* **7**, 6123–6128 (2013).
14. Bai, J. W., Zhong, X., Jiang, S., Huang, Y. & Duan, X. F. Graphene nanomesh. *Nat. Nanotechnol.* **5**, 190–194 (2010).
15. Kim, T. et al. Structural defects in a nanomesh of bulk MoS_2 using an anodic aluminum oxide template for photoluminescence efficiency enhancement. *Sci. Rep.* **8**, 1–6 (2018).
16. Liang, X. G. et al. Formation of bandgap and subbands in graphene nanomeshes with sub-10 nm ribbon width fabricated via nanoimprint lithography. *Nano Lett.* **10**, 2454–2460 (2010).
17. Krishnamoorthy, S., Hinderling, C. & Heinzelmann, H. Nanoscale patterning with block copolymers. *Mater. Today* **9**, 40–47 (2006).
18. Bang, J., Jeong, U., Ryu, D. Y., Russell, T. P. & Hawker, C. J. Block copolymer nanolithography: translation of molecular level control to nanoscale patterns. *Adv. Mater.* **21**, 4769–4792 (2009).
19. Huang, T. et al. Probing the edge-related properties of atomically thin MoS_2 at nanoscale. *Nat. Commun.* **10**, 5544 (2019).
20. Hao, Y., Xu, L. C., Pu, J., Wang, L. & Huang, L. F. Stable zigzag edges of transition-metal dichalcogenides with high catalytic activity for oxygen reduction. *Electrochim. Acta* **338**, 135865 (2020).
21. Yun, T. et al. 2D metal chalcogenide nanopatterns by block copolymer lithography. *Adv. Funct. Mater.* **28**, 1804508 (2018).
22. Su, S. Q. et al. Ultrathin alumina mask-assisted nanopore patterning on mono-layer MoS_2 for highly catalytic efficiency in hydrogen evolution reaction. *ACS Appl. Mater. Interfaces* **10**, 8026–8035 (2018).
23. Davis, S. M. & Carver, J. C. Oxygen chemisorption at defect sites in MoS_2 and ReS_2 basal plane surfaces. *Appl. Surf. Sci.* **20**, 193–198 (1984).
24. Qiu, H. et al. Electrical characterization of back-gated bi-layer MoS_2 field-effect transistors and the effect of ambient on their performances. *Appl. Phys. Lett.* **100**, 123104 (2012).
25. Late, D. J., Liu, B., Matte, H., Dravid, V. P. & Rao, C. N. R. Hysteresis in single-layer MoS_2 field effect transistors. *ACS Nano* **6**, 5635–5641 (2012).
26. Liu, N. et al. Improving the stability of high-performance multilayer MoS_2 field-effect transistors. *ACS Appl. Mater. Interfaces* **9**, 42943–42950 (2017).
27. Kufer, D. & Konstantatos, G. Highly sensitive, encapsulated MoS_2 photodetector with gate controllable gain and speed. *Nano Lett.* **15**, 7307–7313 (2015).
28. Sirota, B., Glavin, N., Krylyuk, S., Davydov, A. V. & Voevodin, A. A. Hexagonal $MoTe_2$ with amorphous BN passivation layer for improved oxidation resistance and endurance of 2D field effect transistors. *Sci. Rep.* **8**, 1–8 (2018).
29. Doherty, J. L., Noyce, S. G., Cheng, Z. H., Abuzaid, H. & Franklin, A. D. Capping layers to improve the electrical stress stability of MoS_2 transistors. *ACS Appl. Mater. Interfaces* **12**, 35698–35706 (2020).
30. Roh, J. et al. Fluorinated CYTOP passivation effects on the electrical reliability of multilayer MoS_2 field-effect transistors. *Nanotechnology* **26**, 455201 (2015).
31. Yoo, H. et al. Highly stacked 3D organic integrated circuits with via-hole-less multilevel metal interconnects. *Nat. Commun.* **10**, 2424 (2019).
32. McDonnell, S. et al. HfO_2 on MoS_2 by atomic layer deposition: adsorption mechanisms and thickness scalability. *ACS Nano* **7**, 10354–10361 (2013).
33. Wells, S. A. et al. Suppressing ambient degradation of exfoliated InSe nanosheet devices via seeded atomic layer deposition encapsulation. *Nano Lett.* **18**, 7876–7882 (2018).
34. Woo, M. H. et al. Low-power nonvolatile charge storage memory based on MoS_2 and an ultrathin polymer tunneling dielectric. *Adv. Funct. Mater.* **27**, 1703545 (2017).
35. Yang, S. C. et al. Large-scale, low-power nonvolatile memory based on few-layer MoS_2 and ultrathin polymer dielectrics. *Adv. Electron. Mater.* **5**, 1800688 (2019).
36. Kong, D. S. et al. Synthesis of MoS_2 and $MoSe_2$ films with vertically aligned layers. *Nano Lett.* **13**, 1341–1347 (2013).
37. Mignuzzi, S. et al. Effect of disorder on Raman scattering of single-layer MoS_2. *Phys. Rev. B* **91**, 195411 (2015).
38. Frey, G. L., Tenne, R., Matthews, M. J., Dresselhaus, M. S. & Dresselhaus, G. Raman and resonance Raman investigation of MoS_2 nanoparticles. *Phys. Rev. B* **60**, 2883–2892 (1999).
39. Brown, N. M. D., Cui, N. Y. & McKinley, A. An XPS study of the surface modification of natural MoS_2 following treatment in an RF-oxygen plasma. *Appl. Surf. Sci.* **134**, 11–21 (1998).
40. Kondekar, N. P., Boebinger, M. G., Woods, E. V. & McDowell, M. T. In situ XPS investigation of transformations at crystallographically oriented MoS_2 interfaces. *ACS Appl. Mater. Interfaces* **9**, 32394–32404 (2017).
41. Yu, S. J. et al. Initiated chemical vapor deposition: a versatile tool for various device applications. *Adv. Eng. Mater.* **20**, 1700622 (2018).
42. Pak, K., Seong, H., Choi, J., Hwang, W. S. & Im, S. G. Synthesis of ultrathin, homogeneous copolymer dielectrics to control the threshold voltage of organic thin-film transistors. *Adv. Funct. Mater.* **26**, 6574–6582 (2016).
43. Oh, J. G. et al. A high-performance top-gated graphene field-effect transistor with excellent flexibility enabled by an iCVD copolymer gate dielectric. *Small* **14**, 1703035 (2018).
44. Li, H. et al. From bulk to monolayer MoS_2: evolution of raman scattering. *Adv. Funct. Mater.* **22**, 1385–1390 (2012).

45. Li, Y., Xu, C. Y., Hu, P. & Zhen, L. Carrier control of MoS$_2$ nanoflakes by functional self-assembled monolayers. *ACS Nano* **7**, 7795–7804 (2013).

46. Lee, S. Y. et al. Large work function modulation of monolayer MoS$_2$ by ambient gases. *ACS Nano* **10**, 6100–6107 (2016).

47. Zschieschang, U. et al. Mixed self-assembled monolayer gate dielectrics for continuous threshold voltage control in organic transistors and circuits. *Adv. Mater.* **22**, 4489–4493 (2010).

48. Sim, D. M. et al. Controlled doping of vacancy-containing few-layer MoS$_2$ via highly stable thiol-based molecular chemisorption. *ACS Nano* **9**, 12115–12123 (2015).

49. Choi, J., Seong, H., Pak, K. & Im, S. G. Vapor-phase deposition of the fluorinated copolymer gate insulator for the p-type organic thin-film transistor. *J. Inf. Disp.* **17**, 43–49 (2016).

50. Yoo, Y., You, J. B., Choi, W. & Im, S. G. A stacked polymer film for robust super-hydrophobic fabrics. *Polym. Chem.* **4**, 1664–1671 (2013).

51. Kim, S. Y., Kim, B. J., Kim, D. H. & Im, S. G. A monolithic integration of robust, water-/oil-repellent layer onto multilayer encapsulation films for organic electronic devices. *RSC Adv.* **5**, 68485–68492 (2015).

52. Chen, X. et al. Degradation behaviors and mechanisms of MoS$_2$ crystals relevant to bioabsorbable electronics. *NPG Asia Mater.* **10**, 810–820 (2018).

53. Di Bartolomeo, A. et al. Hysteresis in the transfer characteristics of MoS$_2$ transistors. *2D Mater.* **5**, 015014 (2018).

AUTHOR CONTRIBUTIONS

H.P., J.C., S.K., S.G.I., and H.Y. conceived the idea and designed the experiments. H.P. fabricated and characterized nanoporous MoS$_2$. H.P. and J.S. measured the electrical properties of passivated and non-passivated nanoporous MoS$_2$ TFTs. J.C. and S.M.L. fabricated the polymer thin films. J.C. analyzed the chemical and surface properties of polymer thin films. H.J.Y. performed XPS/UPS analysis. H.P., J.C., S.K., S.G.I., and H.Y. wrote the manuscript, and all authors reviewed and provided input to the manuscript.

COMPETING INTERESTS

The authors declare no competing interests.

ADDITIONAL INFORMATION

Supplementary information The online version contains supplementary material available at https://doi.org/10.1038/s41699-022-00296-7.

Correspondence and requests for materials should be addressed to Sunkook Kim, Sung Gap Im or Hocheon Yoo.

Reprints and permission information is available at http://www.nature.com/reprints

Publisher's note Springer Nature remains neutral with regard to jurisdictional claims in published maps and institutional affiliations.